Inorganic Chemistry

Article

pubs.acs.org/IC

Phase-Transition Induced Elastic Softening and Band Gap Transition in Semiconducting PbS at High Pressure

Shanmin Wang,[†,‡,§] Jianzhong Zhang,[†] Yi Zhang,[§] Andrew Alvarado,[§] Jeevake Attapattu,[§] Duanwei He,*[,‡] Liping Wang,[§] Changfeng Chen,[§] and Yusheng Zhao*[,†,§]

[†]LANSCE Division, Los Alamos National Laboratory, Los Alamos, New Mexico 87545, United States

[‡]Institute of Atomic & Molecular Physics, Sichuan University, Chengdu 610065, China

[§]HiPSEC & Physics Department, University of Nevada, Las Vegas, Nevada 89154, United States

Supporting Information

ABSTRACT: We have investigated the crystal structure and phase stability, elastic incompressibility, and electronic properties of PbS based on high-pressure neutron diffraction, in-situ electrical resistance measurements, and first-principles calculations. The refinements show that the orthorhombic phase is structurally isotypic with indium iodide (InI) adopting a *Cmcm* structure (*B*33). The cubic-to-orthorhombic transition occurs at ∼2.1(1) GPa with a 3.8% volume collapse and a positive Clausius−Clapeyron slope. Phase-transition induced elastic softening is also observed, which is presumably attributed to the enhanced metallic bonding in the *B*33 phase. On the basis of band structure simulations, the cubic and orthorhombic phases are typical of direct and indirect semiconductors with band gaps of 0.47(1) and 1.04(1) eV, respectively, which supports electrical resistivity measurements of an abrupt jump at the structural transition. On the basis of the resolved structure for *B*33, the phase transition paths for *B*1→*B*33→*B*2 involve translation of a trigonal prism in *B*1 and motion of the next-nearest neighbor Pb atom into {SPb$_7$} coordination and subsequent lattice distortion in the *B*33 phase.

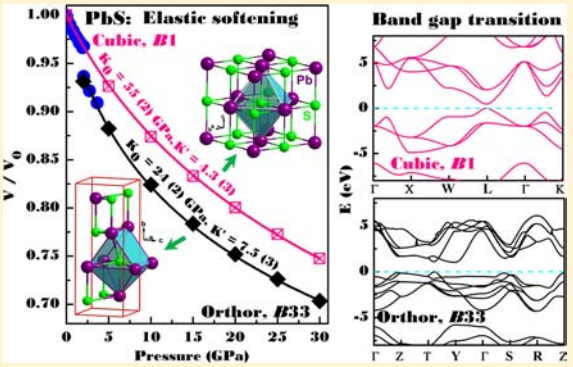

INTRODUCTION

Lead chalcogenides PbX (X = S, Se, and Te) are a class of technologically important semiconductors with narrow band gaps that have widely been used in infrared detectors, diode lasers, thermoelectric devices, and thermophotovoltaic converters.[1−3] Anomalous ferroelectric fluctuations[4,5] and giant anharmonic phonon scattering[5,6] in PbX have recently been discovered and are theoretically attributed to competitive bonding between ionicity and covalency.[7] At atmospheric pressure, these chalcogenides crystallize in a common *NaCl*-type (*B*1) structure. They transform into a *CsCl*-type (*B*2) phase at 13.0−21.5 GPa from an orthorhombic (*orthor*) phase, typically found at lower pressures of 2.2−6.0 GPa.[8−15] Interestingly, pressure-induced *B*1→orthor→*B*2 structural transitions are correlated with electronic transitions of semiconductor → semiconductor → metal.[3,14] However, it is experimentally challenging to accurately determine electronic properties of the orthorhombic and *B*2 phases at high pressures; as a result, they have been the subject of debate and controversy.[3,14,16−18] In fact, pressure-induced phase transition between *B*1 and *B*2 structures has also been observed in binary pnictides (e.g., CeP and CeAs),[19,20] halides (e.g., NaCl and KCl),[21] and hydrides (e.g., NaH and KH).[22,23] A thorough overview of the *B*1→*B*2 transition can be found in ref 24. Elucidation of structural transition between *B*1 and *B*2 is thus of fundamental and technological importance.

The structure of intermediate phase is a key to understanding the pressure-induced *B*1→*B*2 transitions. In most material systems the *B*1−*B*2 transition proceeds without involvement of any intermediate phase.[24] As exceptions, only a few materials have an intermediate phase. Hexagonal structures, for example, have been reported for the *B*1→*B*2 transitions in AgF and NpAs.[25,26] An isostructural transition is observed for SmTe and EuO before transforming to *B*2 modifications at higher pressures.[27] For the cases of lead chalcogenides PbX (X = S, Se, and Te), the *GeS*-type (*B*16, *Pnma* or *Pbnm* (No. 62))[3,11] and *InI*-type (*B*33, *Cmcm* (No. 63))[8,12] structures have both been reported as intermediate phases on the basis of high-pressure synchrotron X-ray diffraction (XRD). On another note, the *B*1→*B*16 (e.g., in NaBr and NaI)[28] and *B*33→*B*2 phase transitions (e.g., in TlI and AgCl)[29,30] are also observed at high pressures, implying that both *B*16 and *B*33 structures are likely candidates for the intermediate phase. However, as pointed out by Knorr et al.,[12] a conclusive resolution of crystal structure between the two structure models is intrinsically difficult based on high-*P* XRD measurements, primarily because

Received: April 1, 2013
Published: July 12, 2013

   dx.doi.org/10.1021/ic400801s | *Inorg. Chem.* 2013, 52, 8638−8643

of significant overlap and broadening of Bragg reflections. Complicating matter further is that a new orthorhombic phase, neither of *GeS*- and *InI*-type structures, has been reported as an intermediate phase in PbTe at 6 GPa.[9] Previous first-principles calculations on the structures of the orthorhombic phase have also been performed, but the results are as conflicting as the experimental reports.[17,18,31,32] In addition, there are significant discrepancies in the elastic bulk modulus (K_0) determined for orthorhombic PbS. The K_0 value measured by Grzechnik et al., for example, is 134(2) GPa,[13] which is more than 300% larger than that reported by Knorr et al. (30.9(4) GPa).[12] A similar discrepancy can also be found in ab initio simulations.[12,31] To date, all these controversies have yet been resolved for the orthorhombic phase, calling for more rigorous investigation into its structural, elastic, and electronic behaviors.

In this work, we carried out high-pressure time-of-flight neutron diffraction, in situ electrical resistance measurements and first-principles calculations on PbS to study its crystal structures, phase stability, elastic and electronic properties. We also proposed new mechanisms for pressure-induced *B*1−*B*2 phase transition in PbS.

EXPERIMENTAL METHODS

High-purity commercially available PbS (>99.99%, ∼50 μm) powders were used for high-pressure (P) and high-temperature (T) neutron diffraction experiments. The time-of-flight experiments were performed in a TAP-98 toroidal-anvil press at Lujan Neutron Scattering Center, Los Alamos Neutron Science Center.[33] Before the experiments, the sample powders were compacted into a cylindrical pellet of 5 mm in diameter and 8 mm in height. A sodium chloride (NaCl) capsule was used to isolate the pellet from the graphite furnace and also served as internal pressure standard. The pressure was determined using a Decker scale of NaCl,[34] and the temperature was measured by a *W5%Re−W26%Rh* thermocouple. The experimental details were described in ref 33. To minimize nonhydrostatic stress built up during room-temperature compression, the sample was annealed at 623 K for 10 min at each experimental pressure before quenching to and collecting data at room-temperature. The obtained neutron diffraction patterns were refined by using a GSAS software.[35]

In situ electrical resistance measurement was carried out in a DS 6 × 8 MN cubic press installed at Sichuan University, China.[36] A pre-compacted cylindrical pellet (1 mm in diameter and 2.5 mm in height) was surrounded by *h*BN pressure-transmitting medium. The electrical connections for resistance measurement are similar to those described in ref 37. At several desired temperatures, electrical resistance data were collected in the pressure range of 0.5−5.0 GPa at a rate of ∼0.2 GPa·min^{-1}. The cell pressure was pre-calibrated by ex situ methods.[36] A chromal-alumal thermocouple was used to monitor the sample temperature. Experimental details can be found elsewhere.[36]

First-principles calculations were performed for PbS using the generalized gradient approximation (GGA-PBE) implemented in the VASP package.[38] The projector augmented-wave (PAW) and pseudopotential methods were employed with a plane-wave basis-set, which was truncated at the cutoff energy of 400 eV to obtain a 0.2 meV convergence in the total energy per atom.[39] The Brillouin zone integration was carried out with a 16 × 16 × 16 k-point grid generated by the Monkhorst−Pack algorithm.[40] The final energy convergence for electronic steps is in the magnitude of 1 μeV. The force convergence of ionic steps was set to be 10 μeV/Å. The spin-orbital interaction was involved for band structure calculations.

RESULTS AND DISCUSSION

Figure 1 shows typical neutron diffraction patterns collected at high-P-T conditions. At room temperature, the onset pressure for the *cubic-to-orthor* transition is determined to be 2.1(1) GPa (see Figure 1b), which agrees well with previously reported

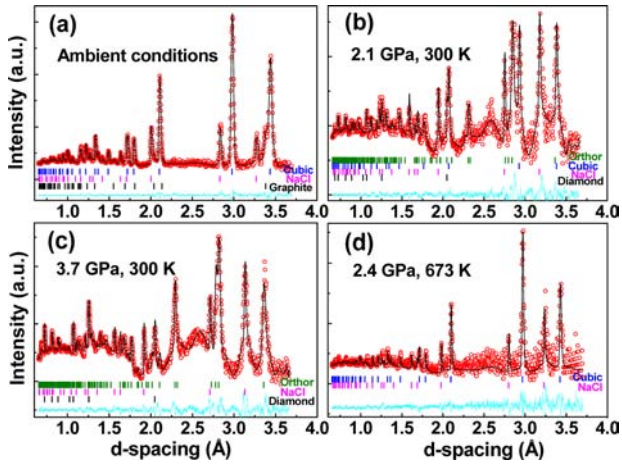

Figure 1. Observed and refined time-of-flight neutron diffraction patterns of PbS at selected high P−T conditions. (**a**) Collected at ambient conditions. The observed diffraction lines for graphite are attributed to the graphite heater. (**b**) At room temperature and 2.1(1) GPa. The *cubic*-to-*orthor* transition occurs at ∼2.1(1) GPa with two PbS phases coexisting up to ∼3.7(1) GPa. (**c**) At room temperature and 3.7(1) GPa. In both (b) and (c), diffraction lines of diamond originate from polycrystalline diamond compact in toroidal-anvil cell.[22] (**d**) At 2.4(1) GPa and 673 K. The orthorhombic PbS is completely back-transformed into the cubic phase. Red circles and black lines denote the observed and calculated profiles, respectively. The difference curves between observed and calculated pattern are shown in cyan. The tick marks correspond to the peak positions.

values.[3,8,11−15] Upon further compression, the relative intensity of orthorhombic phase increases, and at ∼3.7(1) GPa the cubic phase is completely transformed into orthorhombic PbS, as shown in Figure 1c. For comparison, the coexistence of cubic and orthorhombic phases was previously reported between 2.5 and 6.0 GPa by Knorr et al. based on high-P XRD measurements.[12] This is because in our experiment the sample was subjected to high-T annealing before the data collection (see Experimental section for detail), which leads to enhanced kinetics for the cubic-to-orthorhombic transition. To further investigate high-T stability of the orthorhombic phase, we collected neutron diffraction patterns at high temperature. As shown in Figure 1d, the orthorhombic phase disappears at 2.4(1) GPa and 673 K, indicating that the cubic-orthorhombic transition boundary has a positive Clausius−Clapeyron slope.

To determine the crystal structure of the orthorhombic phase, we refine the neutron diffraction pattern collected at 3.7(1) GPa (Figure 1c). Le Bail fitting is initially carried out to refine lattice parameters for both *B*16 and *B*33 structures in advance of Rietveld refinements. The refined results are a = 4.02 (1) Å, b = 11.12 (1) Å, and c = 4.22 (1)Å for *Cmcm* structure, and a = 11.03 (1) Å, b = 4.23 (1) Å, and c = 4.01 (1) Å for *Pnma*. Also noted is that the observed pattern can be fitted very well by using either of *Cmcm* or *Pnma* structure. However, Rietveld refinements of the *Pnma* structure show a large misfit with R_{wp} = 13.4% (the weighted profile R-factor) and χ^2 = 7.7 (goodness of fit). For the *Cmcm* structure, the values of R_{wp} and χ^2 are significantly reduced to 6.5% and 2.2, respectively. Figure 2 shows neutron diffraction patterns calculated for both *Pnma* and *Cmcm* PbS. Obviously, there is some mismatch between the calculated and observed diffraction lines for *Pnma* phase, especially at d-spacing of 2.9 and 3.3 Å. In this simulation the cation and anion positions are fixed respectively at 4*c* (*0.1221*, 1/4, *0.3723*) and 4*c* (*0.3495*, 1/4,

dx.doi.org/10.1021/ic400801s | Inorg. Chem. 2013, 52, 8638−8643

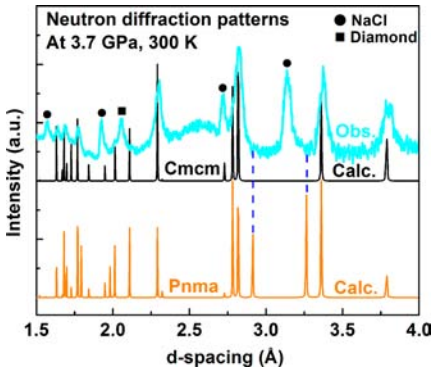

Figure 2. Observed (cyan line) and calculated (dark and orange lines) neutron diffraction patterns for orthorhombic PbS. The observed pattern was collected at 3.7 GPa (see Figure 1c). The calculated patterns are based on *Cmcm* (*B*33) and *Pnma* (*B*16) orthorhombic structures. The structural parameters for *Cmcm* used in simulations are listed in Table 1. For *B*16, simulations are performed by using lattice parameters of a = 11.1288 Å, b = 4.2173 Å, and c = 4.0283 Å. Atomic positions are fixed at Wyckoff sites 4*c* (x, 1/4, z) with x = 0.1221 and z = 0.3723 for cations and x = 0.3495 and z = 0.5023 for anions, which have commonly been reported for *B*16-type GeS and SnS.[11,41,42]

0.5023), which have commonly been reported in *B*16-type GeS and SnS (see Figure 2).[11,41,42] On the other hand, the calculated pattern for *Cmcm* is in excellent agreement with the experimental observations. By using ab initio simulations, the pressure dependence of enthalpy differences for *Cmcm* and *Pnma* PbS are also computed as shown in Figure 3. The

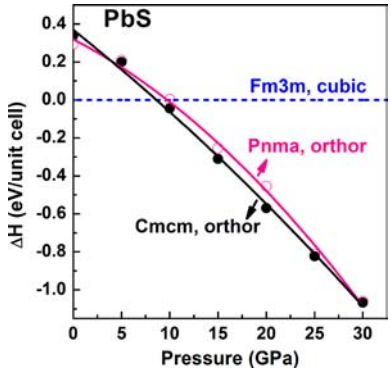

Figure 3. Calculated pressure dependence of enthalpy differences (ΔH) between both orthorhombic and cubic PbS.

calculated phase transition pressures for *Cmcm* and *Pnma* phases are 8.5 (1) and 9.8 (1) GPa, respectively, which are much higher than our experimental observation of 2.1(1) GPa and agree well with previous first-principle simulations.[12,17] Remarkably, *Cmcm* is energetically more favorable to be adopted for the orthorhombic phase than *Pnma* PbS at high pressure. We thus conclude that the orthorhombic PbS is structurally isotypic with indium iodide (InI) adopting the *Cmcm* (*B*33) structure. The final refinement results for selected neutron diffraction patterns are shown in Figure 1. The refined crystal structure parameters for *Cmcm*−PbS are summarized in Table 1. On another note, the obtained figure-of-merit values of the refinements deteriorated with R_{wp} = 9.0% and χ^2 = 4.2 when the atomic positions of Pb and S are exchanged. Coordinates of y_{pb} = 0.3778 and y_s = 0.1363 are thus selected for Wyckoff sites 4*c*(0, y, 1/4) of Pb and S, respectively. The refined atomic

Table 1. Summary of Structural Parameters for Orthorhombic PbS Refined from the Neutron Diffraction Pattern Collected at 3.7 (1) GPa and 300 K[a]

formula	orthorhombic PbS
P−T conditions	3.7 (1) GPa, 300 K
crystal system, space group	orthorhombic, *Cmcm* (No. 63)
strukturbericht designation	*B*33
cell content	Pb_4S_4
cell parameters [Å]	a = 4.0283 (3), b = 11.1288 (7), c = 4.2173 (5)
cell volume [Å^3]	189.063 (4)
density [g·cm^{-3}]	8.4057 (6)
Pb Wyckoff site	4*c*, (0, y, 1/4), y = 0.3778
S Wyckoff site	4*c*, (0, y, 1/4), y = 0.1363
d_{Pb-S} [Å]	2.6882 (2), 2.9203 (3), 3.5121 (3)
d_{Pb-Pb} [Å]	3.4410 (3), 4.0283 (4), 4.0743 (5), 4.2170 (3)
R_{wp} (%), χ^2	6.5, 2.2

[a]See Figure 1c.

positions for *Cmcm*−PbS are consistent with those reported based on density-functional-theory (DFT) calculations.[18]

The pressure−volume (P−V) measurements for cubic and *Cmcm* PbS are illustrated in Figure 4. At ∼2.1 GPa, the cubic-

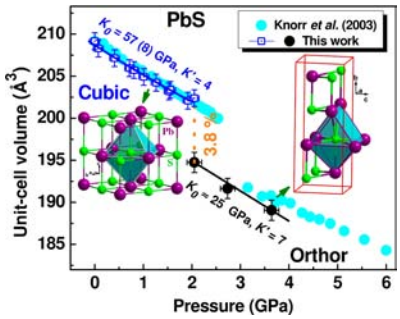

Figure 4. Room-temperature volume-pressure data of *cubic*− (open blue squares) and *orthor*−PbS (solid black circles) obtained from time-of-flight neutron diffraction. The data are fitted to the third-order Birch−Murnaghan equation of state with K', its pressure derivative of K_0, fixed at 4 and 7, respectively, based on the reported values in ref 12 (solid blue line for cubic PbS and black dot line for orthorhombic PbS). Also plotted are experimental observations from ref 12 for comparison purpose (solid cyan circles). Insets are crystal structures of the two phases depicted in polyhedral views.

orthor transition is accompanied by a ∼3.8% volume collapse, indicating that *orthor*-PbS is a high-P phase with a higher density. The ambient bulk modulus K_0, derived from the second-order Birch−Murnaghan equation of state,[43] is 57 (8) GPa for cubic PbS which agrees well with previously reported values (see Figure 4).[12,17] Because of the lack of experimental data, the bulk modulus for *InI*-type PbS cannot be determined accurately in this work; nevertheless, the obtained K_0 value of 25 GPa is comparable with previously published values of 25−34 GPa (see Figure 4).[12,17] Also plotted in Figure 4 are P−V data reported by Knorr et al.,[12] which is in good agreement with our measurements. Strikingly, the high-density orthorhombic phase is more than ∼50% more compressible than the low-P cubic phase. This anomalous elastic softening is against the common physical intuition and has only sparsely been reported in literature. To confirm such behavior, first-principles calculations were performed on PbS, and the calculation methods are described in the Experimental Section. As shown

dx.doi.org/10.1021/ic400801s | Inorg. Chem. 2013, 52, 8638−8643

in Figure 5, the calculated $P-V$ data for both phases are consistent with observations within the experimental pressure

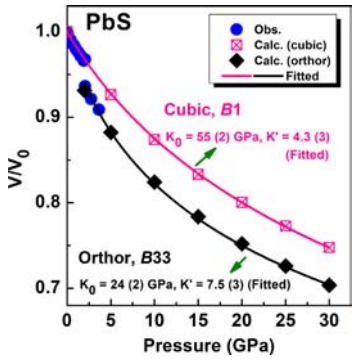

Figure 5. Calculated $P-V$ data for both $B1$ (pink) and $B33$ (black) PbS based on ab initio simulations. For comparison purpose, the measured $P-V$ data are also plotted (solid blue circles).

ranges. The K_0 values, derived from the fit to a third Birch–Murnaghan equation of state,[43] are 55 (2) and 24 (2) GPa, respectively, for the cubic and orthorhombic phases, which agree well with our experimental measurements (see Figure 4) and reported in refs 12 and 17. The derived K', the pressure dependence of K_0, however, is substantially different, 7.5 (3) for the orthorhombic PbS and 4.3 (3) for the cubic phase. To take into account the well-known K_0-K' trade-off, we fitted the $P-V$ data for both phases at a fixed value of $K' = 4$, and we obtain 57 (2) and 30 (8) GPa, respectively, for the cubic and the orthorhombic phases. Thus, for both fitting schemes our simulations support the experimental finding of phase-transition induced elastic softening. For comparison purpose, the K_0 and $P-T$ data are also simulated for *Pnma*–PbS, which are close to those of *Cmcm*–PbS (see Supporting Information, Figure S1).

The refined structural parameters for *cubic*– and *orthor*–PbS at 2.1(1) GPa are listed in Table 2. Notably, three of the four

Table 2. Refined Structural Parameters for Cubic and Orthorhombic PbS at 2.1(1) GPa and 300 K[a]

	cubic, *B1*	orthorhombic, *B33*
$P-T$ conditions	2.1(1) GPa, 300 K	2.1(1) GPa, 300 K
structure	*NaCl*-type, $Fm\bar{3}m$	*InI*-type, *Cmcm*
cell content	Pb_4S_4	Pb_4S_4
cell parameters [Å]	a = 5.8713 (2)	a = 4.1057 (7), b = 11.2215 (9), c = 4.2272 (7)
cell volume [Å^3]	202.393 (5)	194.755 (7)
density [g·cm^{-3}]	7.852 (4)	8.160 (6)
d_{Pb-S} [Å]	2.9360 (2)	2.7103 (3), 2.9510 (4), 3.5544 (5)
d_{Pb-Pb} [Å]	4.1516 (3)	3.4620 (5), 4.1065 (5), 4.1123 (3), 4.2271 (4)

[a]See Figure 1b.

Pb–Pb bonds become shorter upon the transition from *cubic*– to *orthor*–PbS. In particular, the nearest distance between two neighboring Pb atoms is only 3.4620 Å, which is 16.6% shorter than that of cubic phase (4.1516 Å) and is even shorter than the interatomic distance in lead metal (~3.5 Å). The shortest Pb–Pb bond is found in *CsCl*-type metallic PbS, which is ~3.29 Å.[8,17,18] These evidence indicate that chemical bonds in *Cmcm*–PbS are more metallic than in the cubic phase. On the other hand, the Pb atoms in the *Cmcm* phase are 7-fold-coordinated to the S atoms, and it is higher than 6-fold-coordinated $\{PbS_6\}$ octahedrons in cubic PbS (see Figure 4), which is consistent with the pressure-coordination rule.[44,45] To take the argument one step further, the phase-transition-induced elastic softening in PbS may be attributed to such changes in bonding and coordination characteristics at high pressure. Further computational work is warranted to quantify and understand this intriguing phenomenon.

Figure 6 shows electrical resistance (R) of PbS as a function of pressure, $R(P)$, at several different temperatures. A

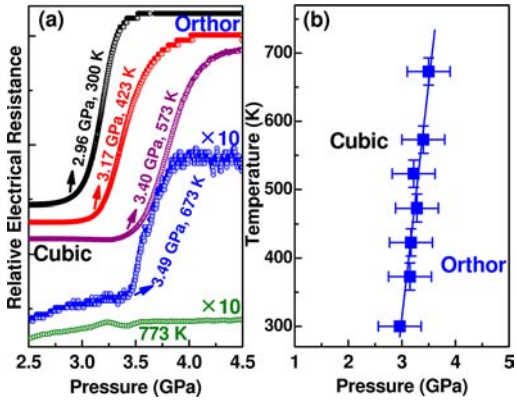

Figure 6. In situ electrical resistance measurements for PbS. (**a**) Electrical resistance as a function of pressure at temperatures of 300 K, 423 K, 573 K, 673 K, and 773 K. The resistance data collected at 673 and 773 K are enlarged ten times (×10) to show detail. (**b**) Cubic-orthorhombic phase boundary for PbS determined based on electrical resistance measurements.

remarkable resistance jump is observed in each of the $R(P)$ curves except for the case at 773 K (Figure 6a). Such discontinuous variations are strong indication of pressure-induced *cubic-to-orthor* phase transition, which is in agreement with previously reported measurements.[3,14,16] At 773 K, no visible resistance jump is observed, implying that the *cubic-to-orthor* phase transition does not occur within the experimental pressure range. As discussed above, orthorhombic PbS is more metallic than cubic phase because of its shorter Pb–Pb bonds. However, contrary to what one might expect, the orthorhombic phase exhibits much lower electrical conductivity than the cubic phase as shown in Figure 6a. This is mainly because electrical conductivities in low-symmetry crystals are often lower than in high-symmetry crystals. In fact, depending on symmetry changes, the structural transition induced electrical resistivity jump or drop have both been reported in the literature.[46] Compared with cubic PbS, the orthorhombic structure possesses a lower crystal symmetry with a "disordered" atomic arrangement. As a result, electrical resistivity increases abruptly during the *cubic-to-orthor* transition in PbS. To gain further insight into such behavior, we performed band structure calculations for both $B1$ and $B33$ phases of PbS (see Experimental Section). As shown in Figure 7, the two phases show remarkable differences in their band structures and total density of states (DOS) at the Fermi energy level (E_f = 0 eV). The cubic phase is a direct band gap semiconductor because the valence-band top and conduction-band bottom occur at the same L symmetry point (see Figure 7 a). The obtained band gap, E_g, is 0.47(1) eV, which is close to the experimental value

dx.doi.org/10.1021/ic400801s | Inorg. Chem. 2013, 52, 8638–8643

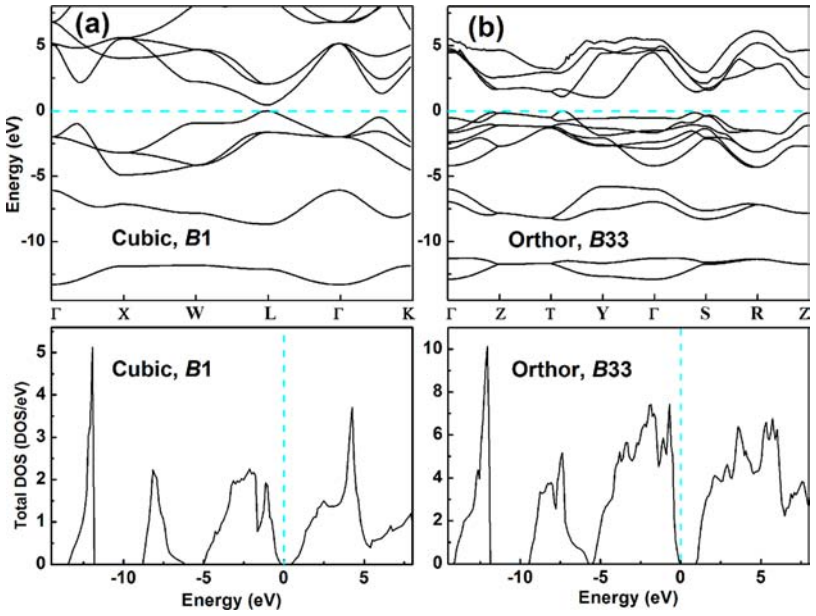

Figure 7. Simulated band structures (upper panel) and total density of state (DOS) (bottom panel) for PbS (**a**) cubic, *B*1 phase, (**b**) orthorhombic, *B*33 phase. Cyan lines denote Fermi energy level (E_f = 0 eV).

of 0.42 eV at 300 K[47,48] and also agrees well with the reported theoretical result.[17] Strikingly, the orthorhombic phase is typical of a semiconductor with an indirect band gap of E_g = 1.04(1) eV (see Figure 7 b), similar to that of silicon (E_g = 1.11 eV at 300 K), one of the well-recognized indirect semiconductors.[49] Thus, our simulations infer a direct-to-indirect band gap transition in semiconducting PbS, which is primarily responsible for the observed electrical resistivity jump (see Figure 6). Band structures of *Pnma*-type PbS are also computed (see Supporting Information, Figure S2). Moreover, on the basis of electrical resistance measurements, the phase boundary for PbS can be determined and is plotted in Figure 6b. The thus-measured transition pressures are slightly higher than those observed in neutron diffraction experiments, which may be attributed to the different pressure calibration methods.

To understand the pressure-induced *B*1→*B*2 phase transition, crystal structures of *B*1-, *B*33-, and *B*2-type PbS are illustrated in polyhedral views in Figure 8. As shown in Figure 8a, the orthorhombic *B*33 phase can simply be viewed as a slight translation of trigonal-prismatic coordination along the (110) crystallographic plane in the *B*1 phase at high pressure. The translation distance is $\sqrt{2}a/4$, where *a* is lattice parameter of the *B*1 phase. For *B*33 → *B*2 transition, as shown in Figure 8b, the motion of the next-nearest neighbor Pb atom into {SPb_7} coordination (see insets in Figure 4) would initially lead to a distorted {SPb_8} coordination in the *B*33 structure. At further higher pressures, the distorted cubic lattice is eventually converted into regular cubic coordination {SPb_8} to form a *CsCl*-type structure.

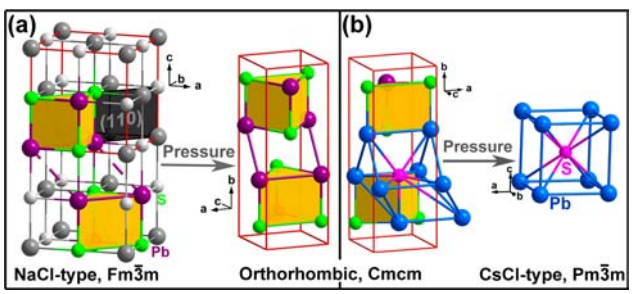

Figure 8. Schematic illustrations of pressure-induced phase transitions in PbS. (**a**) phase transition between *B*1 and *B*33. (**b**) Phase transition between *B*33 and *B*2. Unit cells of the *B*1 and *B*33 phases are outlined in red.

CONCLUSION

In summary, the pressure-induced phase transition in PbS was studied by using time-of-flight neutron diffraction, in situ electrical resistance measurements, and first-principles calculations. The refinements of the neutron diffraction data show that orthorhombic PbS adopts an *InI*-type, *B*33 structure with the *Cmcm* (No. 63) space group . The cubic-to-orthor phase transition starts at 2.1(1) GPa and is accompanied by a ~3.8% volume collapse. On the basis of first-principles calculations, both cubic and orthorhombic phases are semiconductors, but they exhibit features of direct and indirect band gaps, respectively, with E_g = 0.47(1) and 1.04(1) eV. Phase transition induced elastic softening is observed in PbS and is likely to be associated with enhanced metallic Pb−Pb bonding in the orthorhombic phase. Phase transition also leads to an anomalous drop in electrical conductivity in orthorhombic PbS, which is mainly attributed to the lower crystal symmetry and the enlarged band gap in the *Cmcm* phase. Based on the refined structure for *B*33, phase transitions paths for *B*1→*B*33→*B*2 involve translation of a trigonal prism in the *B*1 phase and motion of the next-nearest neighbor Pb atom into {SPb_7} coordination and subsequent lattice distortion in the *B*33 phase.

ASSOCIATED CONTENT

Supporting Information

Further details are given in Figures S1−S2. This material is available free of charge via the Internet at http://pubs.acs.org.

dx.doi.org/10.1021/ic400801s | *Inorg. Chem.* 2013, 52, 8638−8643

AUTHOR INFORMATION

Corresponding Author

*E-mail: (D.H.) DuanweiHe@scu.edu.cn. E-mail: (Y.Z.) Yusheng.Zhao@unlv.edu.

Notes

The authors declare no competing financial interest.

ACKNOWLEDGMENTS

This work has partly benefited from the use of the Lujan Neutron Scattering Center at Los Alamos Neutron Science Center, which is funded by the U.S. Department of Energy's Office of Basic Energy Sciences. This work is also supported by UNLV High Pressure Science and Engineering Center (HiPSEC), which is a DOE NNSA Center of Excellence operated under Cooperative Agreement DE-FC52-06NA27684, and UNLV start-up funding to Y.Z. We thank support from the China 973 Program (Grant 2011CB808205), and the National Natural Science Foundation of China (Grant 11027405). We thank X. Zhou for the electrical resistance measurements.

REFERENCES

(1) Khokhlov, D. *Lead Chalcogenides: Physics and Applications*; Taylor & Francis: New York, 2002.
(2) Pei, Y. Z.; LaLonde, A.; Iwanaga, S.; Snyder, G. J. *Energy Environ. Sci.* **2011**, *4*, 2085−2089.
(3) Ovsyannikov, S. V.; Shchennikov, V. V.; Popova, S. V.; Derevskov, A. Y. *Phys. Status Solidi B* **2003**, *235*, 521−525.
(4) Bozin, E. S.; Malliakas, C. D.; Souvatzis, P.; Proffen, T.; Spaldin, N. A.; Kanatzidis, M. G.; Billinge, S. J. L. *Science* **2010**, *330*, 1660−1663.
(5) Jensen, K. M. Ø.; Božin, E. S.; Malliakas, C. D.; Stone, M. B.; Lumsden, M. D.; Kanatzidis, M. G.; Shapiro, S. M.; Billinge, S. J. L. *Phys. Rev. B* **2012**, *86*, 085313.
(6) Delaire, O.; Ma, J.; Marty, K.; May, A. F.; McGuire, M. A.; Du, M. H.; Singh, D. J.; Podlesnyak, A.; Ehlers, G.; Lumsden, M. D.; Sales, B. C. *Nat. Mater.* **2011**, *10*, 614−619.
(7) Zhang, Y.; Ke, X.; Kent, P. R. C.; Yang, J.; Chen, C. *Phys. Rev. Lett.* **2011**, *107*, 175503.
(8) Chattopadhyay, T.; Vonschnering, H. G.; Grosshans, W. A.; Holzapfel, W. B. *Phys. B & C* **1986**, *139*, 356−360.
(9) Rousse, G.; Klotz, S.; Saitta, A. M.; Rodriguez-Carvajal, J.; McMahon, M. I.; Couzinet, B.; Mezouar, M. *Phys. Rev. B* **2005**, *71*, 224116.
(10) Fujii, Y.; Kitamura, K.; Onodera, A.; Yamada, Y. *Solid State Commun.* **1984**, *49*, 135−139.
(11) Wakabaya., I.; Kobayash., H.; Nagasaki, H.; Minomura, S. *J. Phys. Soc. Jpn.* **1968**, *25*, 227−233.
(12) Knorr, K.; Ehm, L.; Hytha, M.; Winkler, B.; Depmeier, W. *Eur. Phys. J. B* **2003**, *31*, 297−303.
(13) Grzechnik, A.; Friese, K. *J. Phys.: Condens. Matter* **2010**, *22*, 095402.
(14) Jiang, J. Z.; Gerward, L.; Secco, R.; Frost, D.; Olsen, J. S.; Truckenbrodt, J. *J. Appl. Phys.* **2000**, *87*, 2658−2660.
(15) Fan, D.-W.; Zhou, W.-G.; Wei, S.-Y.; Liu, J.; Li, Y.-C.; Jiang, S.; Xie, H.-S. *Chin. Phys. Lett.* **2010**, *27*, 086401.
(16) Wheeler, K. T.; Walker, D.; Johnson, M. C. *Am. J. Sci.* **2007**, *307*, 590−611.
(17) Ahuja, R. *Phys. Status Solidi B* **2003**, *235*, 341−347.
(18) Zagorac, D.; Doll, K.; Schön, J. C.; Jansen, M. *Phys. Rev. B* **2011**, *84*, 045206.
(19) Vedel, I.; Redon, A. M.; Rossatmignod, J.; Vogt, O.; Leger, J. M. *J. Phys. C: Solid State Phys.* **1987**, *20*, 3439−3444.
(20) Werner, A.; Hochheimer, H. D.; Meng, R. L.; Bucher, E. *Phys. Lett. A* **1983**, *97*, 207−209.
(21) Merrill, L. *J. Phys. Chem. Ref. Data* **1977**, *6*, 1205−1252.
(22) Duclos, S. J.; Vohra, Y. K.; Ruoff, A. L.; Filipek, S.; Baranowski, B. *Phys. Rev. B* **1987**, *36*, 7664−7667.
(23) Hochheimer, H. D.; Strossner, K.; Honle, W.; Baranowski, B.; Filipek, F. *J. Less-Common Met.* **1985**, *107*, L13−L14.
(24) Tolédano, P.; Knorr, K.; Ehm, L.; Depmeier, W. *Phys. Rev. B* **2003**, *67*, 144106.
(25) Jamieson, J. C.; Halleck, P. M.; Roof, R. B.; Pistorius, C. *J. Phys. Chem. Solids* **1975**, *36*, 939−944.
(26) Benedict, U.; Dabosseignon, S.; Dufour, C.; Luo, H.; Heathman, S. *J. Nucl. Mater.* **1989**, *166*, 48−55.
(27) Jayaraman, A.; Singh, A. K.; Chatterjee, A.; Devi, S. U. *Phys. Rev. B* **1974**, *9*, 2513−2520.
(28) Yagi, T.; Suzuki, T.; Akimoto, S. *J. Phys. Chem. Solids* **1983**, *44*, 135−140.
(29) Samara, G. A.; Walters, L. C.; Northrop, D. A. *J. Phys. Chem. Solids* **1967**, *28*, 1875−1883.
(30) Kusaba, K.; Syono, Y.; Kikegawa, T.; Shimomura, O. *J. Phys. Chem. Solids* **1995**, *56*, 751−757.
(31) Bencherif, Y.; Boukra, A.; Zaoui, A.; Ferhat, M. *Mater. Chem. Phys.* **2011**, *126*, 707−710.
(32) Ovsyannikov, S. V.; Shchennikov, V. V.; Manakov, A. Y.; Likhacheva, A. Y.; Ponosov, Y. S.; Mogilenskikh, V. E.; Vokhmyanin, A. P.; Ancharov, A. I.; Skipetrov, E. P. *Phys. Status Solidi B* **2009**, *246*, 615−621.
(33) Zhao, Y. S.; von Dreele, R. B.; Morgan, J. G. *High Pressure Res.* **1999**, *16*, 161−177.
(34) Decker, D. L. *J. Appl. Phys.* **1971**, *42*, 3239−&.
(35) Toby, B. H. *J. Appl. Crystallogr.* **2001**, *34*, 210−213.
(36) Wang, S.; He, D.; Wang, W.; Lei, L. *High Pressure Res.* **2009**, *29*, 806−814.
(37) Fang, L. M.; He, D. W.; Chen, C.; Ding, L. Y.; Luo, X. J. *High Pressure Res.* **2007**, *27*, 367−374.
(38) Perdew, J. P.; Burke, K.; Ernzerhof, M. *Phys. Rev. Lett.* **1996**, *77*, 3865−3868.
(39) Kresse, G.; Joubert, D. *Phys. Rev. B* **1999**, *59*, 1758−1775.
(40) Monkhorst, H. J.; Pack, J. D. *Phys. Rev. B* **1976**, *13*, 5188−5192.
(41) Albers, W.; Haas, C.; Ober, H.; Schodder, G. R.; Wasscher, J. D. *J. Phys. Chem. Solids* **1962**, *23*, 215−220.
(42) Wiedemeier, H.; Siemers, P. A. *Z. Anorg. Allg. Chem.* **1977**, *431*, 299−304.
(43) Birch, F. *Phys. Rev.* **1947**, *71*, 809−824.
(44) Neuhaus, A. *Chimia* **1964**, *18*, 93−&.
(45) Kroll, P.; Schroter, T.; Peters, M. *Angew. Chem., Int. Ed.* **2005**, *44*, 4249−4254.
(46) Cannon, J. F. *J. Phys. Chem. Ref. Data* **1974**, *3*, 781−824.
(47) In *Non-Tetrahedrally Bonded Elements and Binary Compounds I*; Madelung, O., Rössler, U., Schulz, M., Eds.; Springer: Berlin, Germany, 1998; Vol. *41C*, pp 1−4.
(48) Zhang, Y.; Ke, X.; Chen, C.; Yang, J.; Kent, P. R. C. *Phys. Rev. B* **2009**, *80*, 024304.
(49) Alex, V.; Finkbeiner, S.; Weber, J. *J. Appl. Phys.* **1996**, *79*, 6943−6946.